Spin splitting of the conduction band by exchange interaction in the valence band through a $k \cdot p$ interband process in ferromagnetic semiconductors

Kenji Hayashida*
Division of Applied Physics, Graduate School of Engineering, Hokkaido University, Sapporo, Hokkaido 060-8628, Japan

Hiroshi Akera
Division of Applied Physics, Faculty of Engineering, Hokkaido University, Sapporo, Hokkaido 060-8628, Japan

(Received 10 February 2022; revised 6 June 2022; accepted 6 June 2022; published 21 June 2022)

The momentum-dependent spin splitting in the conduction band couples orbital motion to spin and enables electrical control of spin. Currently, this control relies on the relativistic spin-orbit interaction (SOI), which limits useful materials to those containing heavy elements. Recently, Naka *et al.* [Nat. Commun. **10**, 4305 (2019)] have found a momentum-dependent spin splitting originating from the exchange interaction, which is expected to extend spintronic materials to those without heavy elements. In this paper, we propose a mechanism of the exchange-induced orbital-spin coupling by extending the $\boldsymbol{k} \cdot \boldsymbol{p}$ theory. As an example, we consider an n-type ferromagnetic semiconductor (nFMS) of T_d point group symmetry with the p-d exchange interaction between an electron in the valence band and the spin of a magnetic ion and evaluate the spin splitting in the conduction band of Γ_6 irreducible representation from the eight-band $\boldsymbol{k} \cdot \boldsymbol{p}$ Hamiltonian. We find that the lowest-order spin splitting in bulk is of the second order of momentum, which results in a nonzero splitting at $k_x = k_y = 0$ in a quantum well with a nonzero quantized momentum k_z. An estimation shows that the p-d exchange interaction is the dominant origin of the conduction-band spin splitting in InFeAs nFMS. We also calculate the intrinsic anomalous Hall conductivity of bulk InFeAs generated by the p-d exchange, which provides both the coupling of orbital motion to spin and that of spin to nFMS magnetization. We find that the p-d exchange-induced Hall conductivity exhibits an accelerated increase with Fe density, in contrast to that produced by the s-d exchange and the Dresselhaus SOI. This finding suggests that the extended $\boldsymbol{k} \cdot \boldsymbol{p}$ mechanism of orbital-spin coupling is expected to help find remarkable phenomena and useful applications in a wide variety of materials and structures.

DOI: 10.1103/PhysRevB.105.235203

I. INTRODUCTION

Spin splitting, which depends on wave vector $\boldsymbol{k}$, of energy bands is induced by the relativistic spin-orbit interaction (SOI) in the absence of space inversion symmetry [1–3]. Spin splitting and the corresponding spin orientation are expressed by the $\boldsymbol{k}$-dependent effective magnetic field (EMF) $\boldsymbol{B}_{\rm eff}^{\rm (SOI)}$. This SOI-induced EMF has been utilized in spintronics [4–8], for example, to electrically generate the spin current [9], spin polarization [10], and spin-orbit torque [7,8,11]. Extensively studied SOI-induced EMFs are those given by the Dresselhaus SOI [12] and the Rashba SOI [13–15] due to bulk and structural inversion asymmetries, respectively. One of theoretical methods to evaluate SOI-induced EMFs is the $\boldsymbol{k} \cdot \boldsymbol{p}$ method [16–19]. This method can provide an analytical perturbative expression of the EMF in terms of band parameters such as bandgaps when the considered spin-split band is well apart from other bands in energy. Such an analytical formula for the EMF and that for the impurity-induced SOI [17–21] will be useful in creating a guideline to experimentally control the EMF [22,23] and in designing spin-related phenomena, such as the extrinsic spin Hall effect in double quantum wells (QWs) [24], spin relaxation in double [25,26] and triple [27] QWs, and the persistent spin helix [28,29].

Recently, authors of a theoretical study in an organic antiferromagnet [30] have discovered the $\boldsymbol{k}$-dependent EMF $\boldsymbol{B}_{\rm eff}^{\rm (exch)}$ produced by the exchange interaction instead of the SOI. This exchange-induced EMF has the possibility of considerably extending the spintronic application to materials consisting of light elements. However, the present theory [30], based on a four-orbital Hubbard model, could not obtain the analytical expression of $\boldsymbol{B}_{\rm eff}^{\rm (exch)}$ in terms of band parameters, which helps to make a guideline to control spintronic properties.

Motivated by the exchange-induced $\boldsymbol{k}$-dependent EMF predicted in the organic antiferromagnet [30], in this paper, we generalize the $\boldsymbol{k} \cdot \boldsymbol{p}$ approach to describe $\boldsymbol{B}_{\rm eff}^{\rm (exch)}$ as well as $\boldsymbol{B}_{\rm eff}^{\rm (SOI)}$ in terms of band parameters. The generalized $\boldsymbol{k} \cdot \boldsymbol{p}$ approach derives the EMF acting on an electron in the conduction band as the combined effect of $\boldsymbol{k} \cdot \boldsymbol{p}$ interband transitions and any spin-dependent interaction in the valence band (Fig. 1). The EMF in this approach is created by three processes: (1) the electron in the conduction band makes a transition to the valence band by the $\boldsymbol{k} \cdot \boldsymbol{p}$ interband term, (2) the electron spin rotates by the spin-dependent interaction in the valence band such as the exchange interaction and the atomic SOI, and (3) the electron returns to the conduction band by the $\boldsymbol{k} \cdot \boldsymbol{p}$ term. The EMF in this mechanism, $\boldsymbol{B}_{\rm eff}^{\rm (exch)}$,

*learning-penguin802@eis.hokudai.ac.jp

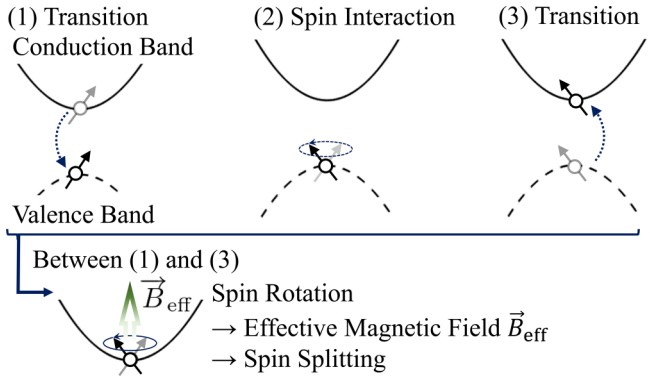

FIG. 1. Mechanism to produce an effective magnetic field (EMF) $\boldsymbol{B}_{\rm eff}$ through (1) and (3) $\boldsymbol{k}\cdot\boldsymbol{p}$ interband transitions [16] with (2) a spin-dependent interaction in a two-band model (conduction and valence bands) for simplicity. The interband transitions (1) and (3) depend on the wave vector $\boldsymbol{k}$, and the spin-dependent interaction in the valence band (2) rotates the spin. The spin rotation of an electron in the conduction band, as a consequence of processes (1)–(3), is expressed by a $\boldsymbol{k}$-dependent EMF $\boldsymbol{B}_{\rm eff}(\boldsymbol{k})$ acting on the electron in the conduction band and leads to the spin splitting.

$\boldsymbol{B}_{\rm eff}^{\rm (SOI)}$, or others, has a $\boldsymbol{k}$ dependence owing to the $\boldsymbol{k}\cdot\boldsymbol{p}$ interband transition as an indispensable process. It is expected that the extended mechanism of the $\boldsymbol{k}$-dependent EMF (Fig. 1) should open the possibility of finding remarkable phenomena and useful applications in a wide variety of materials and structures.

To demonstrate a case where $|\boldsymbol{B}_{\rm eff}^{\rm (exch)}| \gg |\boldsymbol{B}_{\rm eff}^{\rm (SOI)}|$, we apply our extended $\boldsymbol{k}\cdot\boldsymbol{p}$ approach to evaluate $\boldsymbol{B}_{\rm eff}^{\rm (exch)}$ and $\boldsymbol{B}_{\rm eff}^{\rm (SOI)}$ in an n-type ferromagnetic semiconductor (nFMS) of zinc-blende structure with T_d point group symmetry [31–38]. In an FMS the exchange interaction acts between the localized spin of doped magnetic ions and the spin of an electron in energy bands of the semiconductor and produces an indirect ferromagnetic interaction between localized spins, which has been regarded as the origin of the ferromagnetic order in an FMS. We consider the exchange interaction between the localized spin (d orbital) and the electron in the valence band (p orbital) of a semiconductor (p-d exchange interaction) and the atomic SOI in the valence band, as a spin-dependent interaction in process (2) of Fig. 1.

We evaluate the EMF in an nFMS produced by the p-d exchange interaction $\boldsymbol{B}_{\rm eff}^{(p\text{-}d)}$ and that generated by the atomic SOI in the valence band $\boldsymbol{B}_{\rm eff}^{\rm (SOI)}$ from the spin splitting and the spin orientation in the conduction band calculated by the diagonalization of the eight-band $\boldsymbol{k}\cdot\boldsymbol{p}$ Hamiltonian in both a bulk nFMS and a QW structure with an nFMS in the well layer. In addition to this numerical calculation, we also derive the effective Hamiltonian for an electron in the conduction band by treating the $\boldsymbol{k}\cdot\boldsymbol{p}$ interband matrix element in the $\boldsymbol{k}\cdot\boldsymbol{p}$ Hamiltonian as a perturbation [17,19] to obtain analytical approximate formulas of $\boldsymbol{B}_{\rm eff}^{(p\text{-}d)}$ and $\boldsymbol{B}_{\rm eff}^{\rm (SOI)}$. We compare these $\boldsymbol{k}\cdot\boldsymbol{p}$-induced EMFs obtained numerically and analytically with the EMF $\boldsymbol{B}_{\rm eff}^{(s\text{-}d)}$ produced by the s-d exchange interaction between the electron in the conduction band (s orbital) and the localized spin. Elsewhere, $\boldsymbol{B}_{\rm eff}^{(s\text{-}d)}$, which does not depend on $\boldsymbol{k}$, has been used to explain the observed conduction-band spin splitting and the observed Curie temperature of a bulk nFMS [31,37,38].

Our numerical estimation in an InFeAs nFMS shows that $\boldsymbol{B}_{\rm eff}^{(p\text{-}d)}$ is comparable in magnitude with $\boldsymbol{B}_{\rm eff}^{(s\text{-}d)}$ in the bulk and is much larger than the Rashba $\boldsymbol{B}_{\rm eff}^{\rm (SOI)}$ in a QW. The Rashba EMF is one of the origins of electrically generated spin torque on the localized spin. This estimation suggests that (a) the p-d exchange interaction may determine the conduction-band spin splitting and the Curie temperature in nFMSs of InFeAs and others, and (b) $\boldsymbol{B}_{\rm eff}^{(p\text{-}d)}$ can be a promising source of spin torque on the localized spin.

The EMF $\boldsymbol{B}_{\rm eff}^{(p\text{-}d)}$ originating from the p-d exchange interaction in an nFMS, through its $\boldsymbol{k}$ dependence, couples the orbital motion to the spin of an electron in the conduction band. The spin in turn is coupled to the magnetization by the same $\boldsymbol{B}_{\rm eff}^{(p\text{-}d)}$. Therefore, the p-d exchange interaction provides two couplings which are indispensable for the anomalous Hall effect. In this paper, we calculate the intrinsic anomalous Hall conductivity in the bulk InFeAs produced by the p-d exchange interaction. We find that it exhibits a qualitatively different dependence on the Fe dopant concentration compared with the intrinsic anomalous Hall conductivity produced by the Dresselhaus SOI and the coupling to the magnetization through the s-d exchange interaction.

The structure of this paper is as follows. In Sec. II, we perform the symmetry analysis to derive the form of the effective Hamiltonian in the bulk nFMS of T_d point group symmetry for the conduction band of Γ_6 irreducible representation. Section III describes the eight-band $\boldsymbol{k}\cdot\boldsymbol{p}$ Hamiltonian of an nFMS with the zinc-blende structure based on the Zener model of the s-d and p-d exchange interactions. In Sec. IV, we derive the effective Hamiltonian in the conduction band of the bulk and QW systems to obtain analytically approximate formulas of $\boldsymbol{B}_{\rm eff}^{(p\text{-}d)}$ and $\boldsymbol{B}_{\rm eff}^{\rm (SOI)}$. Section V presents the spin splitting and the spin orientation in the bulk and QW of $In_{1-x}Fe_xAs$ at $x = 3.8\%$, which are obtained by numerically calculating eigenvalues and eigenvectors of the $\boldsymbol{k}\cdot\boldsymbol{p}$ Hamiltonian. Here, the analytical $\boldsymbol{B}_{\rm eff}^{(p\text{-}d)}$ of the effective Hamiltonian derived in Sec. IV is employed to explain main features of the spin splitting and the spin orientation numerically presented in this section. In Sec. VI, we numerically calculate the intrinsic anomalous Hall conductivity in the bulk induced by the p-d exchange interaction and the $\boldsymbol{k}\cdot\boldsymbol{p}$ process and demonstrate a feature distinctly different from that induced by the s-d exchange interaction and the Dresselhaus SOI. Finally, Sec. VII presents conclusions.

II. SYMMETRY ANALYSIS OF THE CONDUCTION BAND

First, we derive the form of the effective Hamiltonian for the conduction band in the nFMS of the zinc-blende structure based on the point group of the zinc-blende structure T_d, the irreducible representation of the conduction band Γ_6, and the magnetization introduced as a perturbation. Here, we observe the coupling of the spin $\hat{\boldsymbol{\sigma}}$, the wave vector $\boldsymbol{k}$, and the magnetization $\boldsymbol{M}$ as symmetry-allowed terms, which we will find as p-d exchange-induced orbital-spin coupling by a perturbation calculation in Sec. IV A. To obtain symmetry-adapted terms of the Hamiltonian, we utilize, for example, the

theory of invariants [1,39–41] and retain terms invariant at the time reversal in which $\hat{\boldsymbol{\sigma}}$, $\boldsymbol{k}$, and $\boldsymbol{M}$ reverse the direction. Here, we only consider terms up to the second order of $\boldsymbol{k}$ and the first order of $\boldsymbol{M}$, while the effective Hamiltonian obtained later in Sec. IV A is given up to the second order of $\boldsymbol{k}$ as a nonlinear function of $|\boldsymbol{M}|$.

The derived form of the effective Hamiltonian for the conduction band is

$$\begin{aligned} H_c^{\rm eff} &= (a_{1,1} + a_{1,2}k^2)\hat{1}_\sigma \\ &\quad + (a_{4,1} + a_{4,2}k^2)\sum_{i=x,y,z} M_i\hat{\sigma}_i + a_{4,3}\sum_{i=x,y,z} k_i^2 M_i\hat{\sigma}_i \\ &\quad + a_{4,4}[k_x(k_yM_y + k_zM_z)\hat{\sigma}_x + \text{c.p.}], \end{aligned} \tag{1}$$

where $a_{i,j}$ (following the notation of Refs. [1,39]) is a material-dependent parameter which we can determine by the perturbation calculation in Sec. IV A, $\hat{1}_\sigma$ is a 2×2 identity matrix in spin space, and c.p. means the cyclic permutation of the index. The $a_{1,1}$ term represents a constant energy shift, and the $a_{1,2}$ term corresponds to the kinetic energy. The $a_{4,1}$ term is the coupling of the carrier spin $\hat{\boldsymbol{\sigma}}$ and the magnetization $\boldsymbol{M}$ and corresponds to the s-d exchange interaction in the nFMS. The other terms express the coupling of $\hat{\boldsymbol{\sigma}}$, $\boldsymbol{M}$, and the wave vector $\boldsymbol{k}$. These $\mathbf{k}$-$\hat{\boldsymbol{\sigma}}$-$\boldsymbol{M}$ terms appear through the $\boldsymbol{k}\cdot\boldsymbol{p}$ mechanism (Fig. 1) in the nFMS in which the coupling between $\hat{\boldsymbol{\sigma}}$ and $\boldsymbol{M}$ is provided by the p-d exchange interaction in the valence band, and the $\boldsymbol{k}$ dependence of the coupling is introduced by the $\boldsymbol{k}\cdot\boldsymbol{p}$ transition between the conduction and valence bands. The Dresselhaus SOI and the band nonparabolicity appear when we consider terms of higher order in $\boldsymbol{k}$ [1,39]. For later comparison of Eq. (1) with Eq. (14) by the perturbation calculation in which the magnetization is in the $+z$ direction ($M_z = |\boldsymbol{M}| = M$), we also present a simpler expression in this case:

$$\begin{aligned} H_c^{\rm eff} &= (a_{1,1} + a_{1,2}k^2)\hat{1}_\sigma \\ &\quad + \left(a_{4,1} + a_{4,2}k^2 + a_{4,3}k_z^2\right)M\hat{\sigma}_z \\ &\quad + a_{4,4}k_zM(k_x\hat{\sigma}_x + k_y\hat{\sigma}_y). \end{aligned} \tag{2}$$

III. EIGHT-BAND $\boldsymbol{k}\cdot\boldsymbol{p}$ HAMILTONIAN

The nFMS we consider has the zinc-blende structure, which is shown in Fig. 2(a) for well-studied InFeAs and InFeSb with Fe^{3+} ions substituted for In ions [31]. The exchange interaction between Fe^{3+} spins and conduction-electron spins induces the ferromagnetic phase. Figure 2(b) schematically shows the energy-band structure which exhibits the spin splitting induced by the exchange interaction in both of the conduction and valence bands.

We employ the eight-band Kane model in the $\boldsymbol{k}\cdot\boldsymbol{p}$ approach [16,19] to describe the electronic structure of the nFMS. The $\boldsymbol{k}\cdot\boldsymbol{p}$ approach enables us to focus on the conduction band structure, while first-principles calculations [38,42–46] also present bands originating from Fe^{3+} ions near the conduction band bottom. Table I shows basis vectors to be used for representing the eight-band $\boldsymbol{k}\cdot\boldsymbol{p}$ Hamiltonian in the matrix form. The s-like orbital $|S\rangle$ describes the zone-center state in the conduction band of the host semiconductor, while the p-like orbitals $|X\rangle$, $|Y\rangle$, and $|Z\rangle$ represent those in the valence band. Basis vectors of the spin $|\uparrow\rangle$ and $|\downarrow\rangle$ are eigenvectors of the z component of the spin. Here, x, y, and z axes are taken in [100], [010], and [001] directions, respectively, of the host semiconductor.

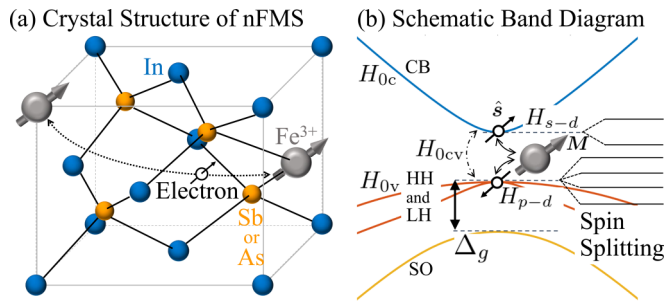

FIG. 2. (a) Crystal structure of n-type ferromagnetic semiconductors (nFMSs) InFeAs and InFeSb. Fe^{3+} spins randomly distributed at In sites form a ferromagnetic phase through s-d and p-d exchange interactions. (b) Schematic energy bands of an nFMS, which exhibit the spin splitting due to s-d and p-d exchange interactions in the conduction band (CB) as well as in the heavy hole (HH), light hole (LH), and split-off (SO) bands (the spin splitting in the SO band is not shown for brevity).

The total $\boldsymbol{k}\cdot\boldsymbol{p}$ Hamiltonian is

$$H = H_0 + H_{\rm ex}. \tag{3}$$

Here, H_0 is the $\boldsymbol{k}\cdot\boldsymbol{p}$ Hamiltonian of the host semiconductor [16,19]:

$$\begin{aligned} H_0 &= \begin{pmatrix} H_{0c} & H_{0cv} \\ H_{0cv}^\dagger & H_{0v} \end{pmatrix}, \\ H_{0c} &= \mathrm{diag}\left(E_k^0,\, E_k^0\right), \\ H_{0v} &= -\mathrm{diag}(E_k',\, E_k',\, E_k',\, E_k',\, \tilde{E}_k,\, \tilde{E}_k), \\ E_k^0 &= \frac{\hbar^2k^2}{2m_0}, \quad E_k' = E_k^0 + E_g, \quad \tilde{E}_k = E_k' + \Delta_g, \\ H_{0cv} &= \left(\sqrt{3}P\boldsymbol{T}\cdot\boldsymbol{k} \quad -\tfrac{1}{\sqrt{3}}P\boldsymbol{\sigma}\cdot\boldsymbol{k}\right). \end{aligned} \tag{4}$$

Here, $\mathrm{diag}[x_1,\, x_2,\, \cdots]$ represents the diagonal matrix with diagonal elements $x_1,\, x_2,\, \cdots$; $\hbar$ is the Planck constant divided by 2π; m_0 is the electron mass in vacuum; E_g and Δ_g are the

TABLE I. Basis vectors for the representation of the $\boldsymbol{k}\cdot\boldsymbol{p}$ Hamiltonian [Eqs. (4) and (5)].

Band	Vector
CB	$\lvert S,\uparrow\rangle$
CB	$\lvert S,\downarrow\rangle$
HH	$-\frac{1}{\sqrt{2}}(\lvert X,\uparrow\rangle + i\lvert Y,\uparrow\rangle)$
LH	$-\frac{1}{\sqrt{6}}(\lvert X,\downarrow\rangle + i\lvert Y,\downarrow\rangle) + \sqrt{\frac{2}{3}}\lvert Z,\uparrow\rangle$
LH	$\frac{1}{\sqrt{6}}(\lvert X,\uparrow\rangle - i\lvert Y,\uparrow\rangle) + \sqrt{\frac{2}{3}}\lvert Z,\downarrow\rangle$
HH	$\frac{1}{\sqrt{2}}(\lvert X,\downarrow\rangle - i\lvert Y,\downarrow\rangle)$
SO	$-\frac{1}{\sqrt{3}}(\lvert X,\downarrow\rangle + i\lvert Y,\downarrow\rangle) - \frac{1}{\sqrt{3}}\lvert Z,\uparrow\rangle$
SO	$-\frac{1}{\sqrt{3}}(\lvert X,\uparrow\rangle - i\lvert Y,\uparrow\rangle) + \frac{1}{\sqrt{3}}\lvert Z,\downarrow\rangle$

bandgap and the split-off gap at the zone center [Fig. 2(b)], respectively; $\boldsymbol{T} = (T_x, T_y, T_z)$ are matrices appearing in the eight-band Kane model [1] (see Appendix B for their explicit forms); $\boldsymbol{\sigma} = (\sigma_x, \sigma_y, \sigma_z)$ are 2×2 Pauli matrices; and P is the Kane matrix element. Here, we have replaced E_k^0 in diagonal elements of H_{0v} of the original eight-band Kane model with $-E_k^0$ since the original E_k^0 in H_{0v} leads to the incorrect convexity of the valence bands [47]. This modification in diagonal elements of H_{0v} can be thought to consider, in the simplest way, the renormalization of band parameters due to remote bands [1]. We neglect the change in the lattice constant due to Fe doping because no significant strains have been observed in experiments [31–38].

Here, $H_{\rm ex}$ represents the s-d and p-d exchange interactions in the Zener model. The Zener model of the exchange interaction has been employed in many theories [5,48–52] to describe the ferromagnetic phase (see Appendix A). In deriving the exchange-induced $\boldsymbol{k}$-dependent EMF in this paper, we also employ the Zener model to take advantage of its simplicity. Then $H_{\rm ex}$ is given by

$$H_{\rm ex} = \begin{pmatrix} H_{s\text{-}d} & O_{cv} \\ O_{cv}^\dagger & H_{p\text{-}d} \end{pmatrix}, \tag{5}$$

$$H_{s\text{-}d} = 3A_{s\text{-}d}\hat{\boldsymbol{\sigma}}^{(s)} \cdot \boldsymbol{e},$$

$$H_{p\text{-}d} = 3B_{p\text{-}d}\hat{\boldsymbol{\sigma}}^{(p)} \cdot \boldsymbol{e}, \tag{6}$$

$$\hat{\sigma}_i^{(s)} = \sigma_i,$$

$$\hat{\sigma}_i^{(p)} = \frac{1}{3}\begin{pmatrix} 2J_i & -6T_i^\dagger \\ -6T_i & -\sigma_i \end{pmatrix},$$

$$i = x, y, z,$$

$$A_{s\text{-}d} = \frac{J_{s\text{-}d}M}{6g\mu_{\rm B}},$$

$$B_{p\text{-}d} = \frac{J_{p\text{-}d}M}{6g\mu_{\rm B}},$$

$$M = |\boldsymbol{M}| = xN_0 g\mu_{\rm B} S. \tag{7}$$

Here, O_{cv} is the 2×6 matrix whose elements are all zero: $\hat{\boldsymbol{\sigma}}^{(s)}$ and $\hat{\boldsymbol{\sigma}}^{(p)}$ are the spin matrices for conduction and valence bands [heavy hole (HH), light hole (LH), and spin off (SO)], respectively: J_x, J_y, and J_z are matrices of the Kane model [1] (see Appendix B for their explicit forms); and $\boldsymbol{e}$ is a unit vector in the direction of the magnetization $\boldsymbol{e} = \boldsymbol{M}/|\boldsymbol{M}|$. In $A_{s\text{-}d}$ and $B_{p\text{-}d}$, M represents the magnitude of magnetization. Here, g and $\mu_{\rm B}$ are the g factor and Bohr magneton; x is the fraction of Fe^{3+} in the cation site; N_0 is the number of the cation site per unit volume; and S is the length of the localized spin. Note that $N_0 J_{s\text{-}d}$ and $N_0 J_{p\text{-}d}$ have dimensions of energy and represent coefficients of s-d and p-d exchange interactions, respectively.

Here, we used the assumption of the saturated magnetization, which is valid at temperatures lower than the ferromagnetic transition temperature.

A. Application to the QW

In applying the $\boldsymbol{k} \cdot \boldsymbol{p}$ Hamiltonian to a QW structure, we consider the quantum confinement in the growth direction [17,19]. We choose the growth direction (z axis) along [001] of the host semiconductor and replace the wave number k_z in the $\boldsymbol{k} \cdot \boldsymbol{p}$ Hamiltonian [Eq. (4)] with the operator $\hat{k}_z = -i\partial/\partial z$.

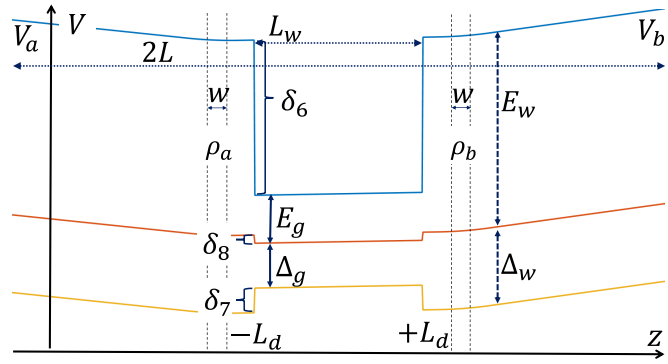

FIG. 3. Quantum well (QW) structure. For details of parameters, see Sec. V A and Table II.

Figure 3 shows our QW structure with band offsets between different layers δ_6, δ_8, and δ_7. In addition to the potential step due to the band offsets, we consider the potential produced by the gate $V_{\rm gate}(z)$, that due to donors $V_{\rm donor}(z)$, and the Hartree potential $V_{\rm Hartree}(z)$ as well as the z dependence of $A_{s\text{-}d}(z)$ and $B_{p\text{-}d}(z)$, which corresponds to the uniform distribution of Fe^{3+} ions within the well layer. These can be incorporated into the $\boldsymbol{k} \cdot \boldsymbol{p}$ Hamiltonian, H_0 in Eq. (4) and $H_{\rm ex}$ in Eq. (5), by the following replacement:

$$\begin{aligned} A_{s\text{-}d} &\to A_{s\text{-}d}(z), \\ B_{p\text{-}d} &\to B_{p\text{-}d}(z), \\ E_k^0 &\to E_k^0 + V_H(z) + h_6(z), \\ -E_k' &\to -E_k' + V_H(z) - h_8(z), \\ -\tilde{E}_k &\to -\tilde{E}_k + V_H(z) - h_7(z), \end{aligned} \tag{8}$$

in which

$$\begin{aligned} V_H(z) &= V_{\rm gate}(z) + V_{\rm donor}(z) + V_{\rm Hartree}(z), \\ h_i(z) &= \delta_i h_{\rm w}(z), \qquad i = 6, 7, 8, \\ h_{\rm w}(z) &= 0 \text{ (inside well)}, 1 \text{ (outside well)}. \end{aligned}$$

IV. EFFECTIVE HAMILTONIAN IN THE CONDUCTION BAND

We derive the effective Hamiltonian for an electron in the conduction band of both the bulk and QW systems, by using the folding-down method [17,19]. Here, we choose the magnetization direction $\boldsymbol{e}$ to be in the $+z$ direction for simplicity [53].

A. Effective Hamiltonian in the bulk

The reduced Hamiltonian for the conduction-band component of the eigenvector is given by

$$\begin{aligned} H_c^{\rm eff} &= H_c + H_{0cv}(E - H_v)^{-1}H_{0cv}^\dagger, \\ H_c &= H_{0c} + H_{s\text{-}d}, \\ H_v &= H_{0v} + H_{p\text{-}d}, \end{aligned} \tag{9}$$

in which E is the eigenenergy of the $\boldsymbol{k}\cdot\boldsymbol{p}$ Hamiltonian. To obtain the effective Hamiltonian without E [17,19], we expand $H_c^{\rm eff}$ in powers of $\chi_8^{\pm 3}$, $\chi_8^{\pm}$, and $\chi_7^{\pm}$ defined by

$$\chi_8^{\pm 3} = \frac{E + E_k^0}{E_g \pm 3B_{p\text{-}d}},$$
$$\chi_8^{\pm} = \frac{E + E_k^0}{E_g \pm B_{p\text{-}d}},$$
$$\chi_7^{\pm} = \frac{E + E_k^0}{E_g + \Delta_g \pm B_{p\text{-}d}},$$

and retain the lowest order by assuming

$$\chi_8^{\pm 3},\ \chi_8^{\pm},\ \chi_7^{\pm} \ll 1. \tag{10}$$

The conditions [Eq. (10)] are satisfied when $E_g - 3|B_{p\text{-}d}| \gg |E + E_k^0|$. InFeAs at $x = 3.8\%$ has $E_g = 0.418$ eV, $\Delta_g = 0.39$ eV, and $3|B_{p\text{-}d}| = 0.11$ eV [42]. In the vicinity of $x = 14\%$, however, $E_g - 3|B_{p\text{-}d}|$ vanishes, and one of the conditions [Eq. (10)] is no longer satisfied. When we investigate InFeAs at $0 < x < 10\%$ in Sec. VI, we will employ the original $\boldsymbol{k}\cdot\boldsymbol{p}$ Hamiltonian [Eq. (3)].

The second term of $H_c^{\rm eff}$ in Eq. (9) is expanded as

$$[H_{0cv}(E - H_v)^{-1}H_{0cv}^{\dagger}]_{(1,1)} = \frac{P^2}{3}\Gamma_1^+ k_{\parallel}^2 + \frac{P^2}{3}\tilde{\Gamma}_1^+ k_z^2,$$
$$[H_{0cv}(E - H_v)^{-1}H_{0cv}^{\dagger}]_{(1,2)} = -\frac{P^2}{3}\tilde{\Gamma}_2 k_z (k_x\hat{\sigma}_x + k_y\hat{\sigma}_y)_{(1,2)},$$

with $k_{\parallel}^2 = k_x^2 + k_y^2$. Here,

$$\Gamma_1^+ = \frac{3}{2}\frac{1}{E_g - 3B_{p\text{-}d}}\left[1 - \chi_8^{-3} + \left(\chi_8^{-3}\right)^2 - \cdots\right] + \frac{1}{2}\frac{1}{(E_g + B_{p\text{-}d})d^+}\left(-\frac{E_g + \Delta_g + 3B_{p\text{-}d}}{E_g + \Delta_g - B_{p\text{-}d}} - \chi_7^-\right) + \frac{1}{(E_g + \Delta_g - B_{p\text{-}d})d^+}\left(-\frac{E_g + 3B_{p\text{-}d}}{E_g + B_{p\text{-}d}} - \chi_8^+\right), \tag{11}$$

$$\tilde{\Gamma}_1^+ = \frac{2}{(E_g - B_{p\text{-}d})d^-}\left(-\frac{E_g + \Delta_g + 3B_{p\text{-}d}}{E_g + \Delta_g + B_{p\text{-}d}} - \chi_7^+\right) + \frac{1}{(E_g + \Delta_g + B_{p\text{-}d})d^-}\left(-\frac{E_g + 3B_{p\text{-}d}}{E_g - B_{p\text{-}d}} - \chi_8^-\right), \tag{12}$$

$$\tilde{\Gamma}_2 = -\frac{\Delta_g - (E_g + \Delta_g + B_{p\text{-}d})\chi_7^+ + (E_g - B_{p\text{-}d})\chi_8^-}{(E_g - B_{p\text{-}d})(E_g + \Delta_g + B_{p\text{-}d})d^-} + \frac{\Delta_g - (E_g + \Delta_g - B_{p\text{-}d})\chi_7^- + (E_g + B_{p\text{-}d})\chi_8^+}{(E_g + B_{p\text{-}d})(E_g + \Delta_g - B_{p\text{-}d})d^+},$$

$$d^{\pm} = \frac{(2\sqrt{2}B_{p\text{-}d})^2}{(E_g \pm B_{p\text{-}d})(E_g + \Delta_g \mp B_{p\text{-}d})} - (1 + \chi_8^{\pm}\chi_7^{\mp} + \chi_8^{\pm}\chi_7^{\mp}). \tag{13}$$

We can obtain the $[H_{0cv}(E - H_v)^{-1}H_{0cv}^{\dagger}]_{(2,2)}$ component by flipping the sign in front of $B_{p\text{-}d}$ in the $[H_{0cv}(E - H_v)^{-1}H_{0cv}^{\dagger}]_{(1,1)}$ component. Here, we assume the conditions [Eq. (10)] and retain the zeroth order of $\chi_8^{\pm 3}$, $\chi_8^{\pm}$, and $\chi_7^{\pm}$ [19].

Then we obtain the effective Hamiltonian given by

$$H_c^{\rm eff} = \frac{\varepsilon_{\boldsymbol{k}\uparrow} + \varepsilon_{\boldsymbol{k}\downarrow}}{2}\hat{1}_\sigma + 3A_{s\text{-}d}\hat{\sigma}_z + \boldsymbol{B}_{\rm eff}^{(p\text{-}d)}\cdot\hat{\boldsymbol{\sigma}}. \tag{14}$$

Here, $\boldsymbol{B}_{\rm eff}^{(p-d)}$ is the EMF due to the p-d exchange interaction given by

$$\left[\boldsymbol{B}_{\rm eff}^{(p\text{-}d)}\right]_\mu = -\frac{1}{3}P^2\tilde{\Gamma}_2 k_z k_\mu,$$
$$\left[\boldsymbol{B}_{\rm eff}^{(p\text{-}d)}\right]_z = \frac{\varepsilon_{\boldsymbol{k}\uparrow} - \varepsilon_{\boldsymbol{k}\downarrow}}{2},$$
$$\mu = x, y, \tag{15}$$

and $\varepsilon_{\boldsymbol{k}\sigma}$ ($\sigma = \uparrow, \downarrow$) is the spin-dependent kinetic energy expressed by

$$\varepsilon_{\boldsymbol{k}\sigma} = \frac{\hbar^2 k_{\parallel}^2}{2m_{\parallel\sigma}^*} + \frac{\hbar^2 k_z^2}{2m_{z\sigma}^*}. \tag{16}$$

Then the eigenenergies $E_\pm$ are obtained to be

$$E_\pm = \frac{E_{\boldsymbol{k}\uparrow} + E_{\boldsymbol{k}\downarrow}}{2} \pm \Delta E, \tag{17}$$
$$E_{\boldsymbol{k}\sigma} = \varepsilon_{\boldsymbol{k}\sigma} + 3A_{s\text{-}d}\sigma,$$
$$\Delta E = \sqrt{\left(\frac{E_{\boldsymbol{k}\uparrow} - E_{\boldsymbol{k}\downarrow}}{2}\right)^2 + \left(\frac{P^2}{3}\tilde{\Gamma}_2\right)^2 k_{\parallel}^2 k_z^2}. \tag{18}$$

Spin-dependent effective masses and $\tilde{\Gamma}_2$ are given by

$$\frac{m_0}{m_{\parallel\uparrow}^*} = 1 + \frac{r_-}{2} + \frac{R_+ + E_P g_+}{6},$$
$$\frac{m_0}{m_{z\uparrow}^*} = 1 + \frac{R_- + 2E_P g_-}{3},$$
$$\frac{m_0}{m_{\parallel\downarrow}^*} = 1 + \frac{r_+}{2} + \frac{R_- + E_P g_-}{6},$$
$$\frac{m_0}{m_{z\downarrow}^*} = 1 + \frac{R_+ + 2E_P g_+}{3}, \tag{19}$$
$$\tilde{\Gamma}_2 = g_- - g_+, \tag{20}$$

with

$$E_P = \frac{2m_0P^2}{\hbar^2},$$
$$r_\pm = \frac{E_P}{E_g \pm 3B_{p\text{-}d}},$$
$$R_\pm = \frac{E_P(3E_g \pm 9B_{p\text{-}d})}{\delta_\pm},$$
$$g_\pm = \frac{\Delta_g}{\delta_\pm},$$
$$\delta_\pm = (E_g \pm B_{p\text{-}d})(E_g + \Delta_g \mp B_{p\text{-}d}) - 8B_{p\text{-}d}^2. \tag{21}$$

These expressions show that $\tilde{\Gamma}_2$ and $\varepsilon_{\boldsymbol{k}\sigma}$ depend nonlinearly on the magnetization M through $B_{p\text{-}d} \propto M$ [Eq. (7)]. Therefore, $\boldsymbol{B}_{\rm eff}^{(p\text{-}d)}$ is a nonlinear function of M.

The correspondence between coefficients of the symmetry-adapted terms in Eq. (2) and those of the effective Hamiltonian

in Eq. (14) is

$$\begin{aligned} a_{1,1} &= 0, \\ a_{1,2}k^2 &= \frac{\varepsilon_{\boldsymbol{k}\uparrow} + \varepsilon_{\boldsymbol{k}\downarrow}}{2}, \\ a_{4,1}M &= 3A_{s\text{-}d}, \\ a_{4,2}M &= \frac{\hbar^2}{4}\left(\frac{1}{m^*_{\parallel\uparrow}} - \frac{1}{m^*_{\parallel\downarrow}}\right), \\ a_{4,3}M &= \frac{\hbar^2}{4}\left(\frac{1}{m^*_{z\uparrow}} - \frac{1}{m^*_{z\downarrow}}\right) - a_{4,2}M, \\ a_{4,4}M &= -\frac{1}{3}P^2\tilde{\Gamma}_2. \end{aligned} \tag{22}$$

Here, the right-hand side of each equation is to be considered up to the first order of M since the symmetry-adapted terms in Eq. (2) are derived up to this order.

The EMF $\boldsymbol{B}^{(p\text{-}d)}_{\rm eff}$ obtained in Eq. (15) is of the second order of wave vector $\boldsymbol{k}$. The x and y components are proportional to k_zk_x and k_zk_y, respectively, and the z component is expressed by the difference in kinetic energy between spin-up and spin-down states. The $\boldsymbol{k}$-quadratic $\boldsymbol{B}^{(p\text{-}d)}_{\rm eff}$ is in remarkable contrast with the $\boldsymbol{k}$-linear and $\boldsymbol{k}$-cubic EMFs of the Rashba and Dresselhaus SOIs, respectively. The SOIs in nonmagnetic semiconductors must be of odd order of $\boldsymbol{k}$ due to the time-reversal symmetry. On the other hand, $\boldsymbol{B}^{(p\text{-}d)}_{\rm eff}$ must be of even order of $\boldsymbol{k}$ because $\boldsymbol{B}^{(p\text{-}d)}_{\rm eff}$ reverses the direction with the magnetization reversal.

The z component of $\boldsymbol{B}^{(p\text{-}d)}_{\rm eff}$, which appears in the presence of $B_{p\text{-}d}$ giving the spin dependence of effective masses $m^*_{\parallel\sigma}$ and $m^*_{z\sigma}$, originates from the magnetization along the z direction. The x and y components, which are proportional to $\tilde{\Gamma}_2$, are induced by Δ_g, the spin-orbit splitting in the valence band, in addition to $B_{p\text{-}d}$. The direction of these components in the xy plane perpendicular to the magnetization is that parallel to $(k_x, k_y, 0)$ in contrast to the Rashba EMF, which is perpendicular to $(k_x, k_y, 0)$. Figures 4(a) and 4(b) schematically depict

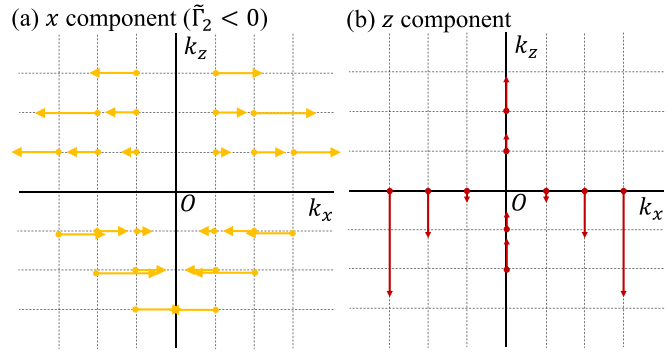

FIG. 4. Effective magnetic field (schematic) due to the p-d exchange interaction $\boldsymbol{B}^{(p\text{-}d)}_{\rm eff}$ given in Eq. (15). (a) x and (b) z components in the k_xk_z plane with O the $\boldsymbol{k} = \boldsymbol{0}$ point in the case of $B_{p\text{-}d} < 0$ (see Table II), which gives $\tilde{\Gamma}_2 < 0$ and $1/m^*_{\parallel\uparrow} - 1/m^*_{\parallel\downarrow} \simeq -2(1/m^*_{z\uparrow} - 1/m^*_{z\downarrow}) < 0$. The latter leads to $\varepsilon_{\boldsymbol{k}\uparrow} < \varepsilon_{\boldsymbol{k}\downarrow}$ for $\boldsymbol{k}$ in the k_xk_y plane and $\varepsilon_{\boldsymbol{k}\uparrow} > \varepsilon_{\boldsymbol{k}\downarrow}$ for $\boldsymbol{k}$ along the k_z axis.

x and z components, respectively, of $\boldsymbol{B}^{(p\text{-}d)}_{\rm eff}$ in the k_xk_z plane when $\tilde{\Gamma}_2 < 0$ and $1/m^*_{\parallel\uparrow} - 1/m^*_{\parallel\downarrow} \simeq -2(1/m^*_{z\uparrow} - 1/m^*_{z\downarrow}) < 0$, which are both satisfied for $B_{p\text{-}d} < 0$. The y component is zero since $k_y = 0$.

B. Effective Hamiltonian in the QW

By expanding $H^{\rm eff}_c$ [Eq. (9)] adjusted to the QW [Eq. (8)] in powers of

$$\chi^{\pm3}_8 = \frac{E - \left[-\frac{\hbar^2}{2m_0}\left(k^2_\parallel + \hat{k}^2_z\right) + V_H(z) - h_8(z)\right]}{E_g \pm 3B_{p\text{-}d}(z)},$$

$$\chi^{\pm}_8 = \frac{E - \left[-\frac{\hbar^2}{2m_0}\left(k^2_\parallel + \hat{k}^2_z\right) + V_H(z) - h_8(z)\right]}{E_g \pm B_{p\text{-}d}(z)},$$

$$\chi^{\pm}_7 = \frac{E - \left[-\frac{\hbar^2}{2m_0}\left(k^2_\parallel + \hat{k}^2_z\right) + V_H(z) - h_7(z)\right]}{E_g + \Delta_g \pm B_{p\text{-}d}(z)},$$

we obtain for the second term of $H^{\rm eff}_c$ in Eq. (9):

$$[H_{0cv}(E - H_v)^{-1}H^\dagger_{0cv}]_{(1,1)} = \frac{P^2}{3}\Gamma^+_1(z)k^2_\parallel + \frac{P^2}{3}\hat{k}_z\tilde{\Gamma}^+_1(z)\hat{k}_z,$$

$$[H_{0cv}(E - H_v)^{-1}H^\dagger_{0cv}]_{(1,2)} = \frac{P^2}{3}\frac{d\Gamma_2(z)}{dz}(k_y\hat{\sigma}_x - k_x\hat{\sigma}_y)_{(1,2)} - \frac{P^2}{3}\tilde{\Gamma}_2(z)\hat{k}_z(k_x\hat{\sigma}_x + k_y\hat{\sigma}_y)_{(1,2)}.$$

$$\Gamma_2(z) = \frac{-\Delta_g - (E_g + \Delta_g + B_{p\text{-}d})\chi^+_7 + (E_g - B_{p\text{-}d})\chi^-_8}{(E_g - B_{p\text{-}d})(E_g + \Delta_g + B_{p\text{-}d})d^-}.$$

Here, the z dependence in the QW of the material parameters E_g, Δ_g, and $B_{p\text{-}d}$ are considered in Γ^+_1 [Eq. (11)], $\tilde{\Gamma}^+_1$ [Eq. (12)], Γ_2, and $\tilde{\Gamma}_2$ [Eq. (13)].

Then in the lowest order of $\chi^{\pm3}_8$, $\chi^{\pm}_8$, and $\chi^{\pm}_7$, we obtain the operator for the EMF $\hat{\boldsymbol{B}}^{\rm QW}_{\rm eff}$ given by

$$\left(\hat{\boldsymbol{B}}^{\rm QW}_{\rm eff}\right)_x = -\frac{P^2}{3}\{\hat{A}k_x - [\hat{B} + C(z)]k_y\}, \tag{23}$$

$$\left(\hat{\boldsymbol{B}}^{\rm QW}_{\rm eff}\right)_y = -\frac{P^2}{3}\{\hat{A}k_y + [\hat{B} + C(z)]k_x\}, \tag{24}$$

$$\hat{A} = \frac{1}{2}[\tilde{\Gamma}_2(z), \hat{k}_z], \quad \hat{B} = \frac{i}{2}[\tilde{\Gamma}_2(z), \hat{k}_z],$$

$$\left(\hat{\boldsymbol{B}}^{\rm QW}_{\rm eff}\right)_z = \frac{\hat{\varepsilon}_\uparrow - \hat{\varepsilon}_\downarrow}{2}, \quad \hat{\varepsilon}_\sigma = \frac{\hbar^2k^2_\parallel}{2m^*_{\parallel\sigma}(z)} + \frac{\hbar^2}{2}\hat{k}_z\frac{1}{m^*_{z\sigma}(z)}\hat{k}_z. \tag{25}$$

TABLE II. Parameter values used in the calculation in the bulk InFeAs (Fig. 2) and the QW AlSb/InFeAs/AlSb (Fig. 3) at the Fe^{3+} fraction of $x = 3.8\%$. Units of energy and length are electronvolts and nanometers, respectively. The doping densities are $\rho_a = \rho_b = 1 \times 10^{18}$ cm^{-3}. The temperature T is 30 K, which is lower than the Curie temperature of InFeAs [32–38], which is 40 K at $x = 5\%$. The boundary potentials are chosen to be $V_a = 0$ and $V_b = 0.1$ eV. The bias of 0.1 eV gives rise to ∼1 meV Rashba spin splitting.

$E_g = 0.418$	$\Delta_g = 0.390$	$E_P = 21.5$
$6A_{s\text{-}d} = 0$ or 0.02	$6B_{p\text{-}d} = -0.22$	$\delta_6 = 1.35$
$E_w = 1.696$	$\Delta_w = 0.676$	$L = 40$
$L_d = 18$	$w = 6$	$L_w = 20$

where $\{\hat{X}_1, \hat{X}_2\} = \hat{X}_1\hat{X}_2 + \hat{X}_2\hat{X}_1$ and $[\hat{X}_1, \hat{X}_2] = \hat{X}_1\hat{X}_2 - \hat{X}_2\hat{X}_1$. Here, terms with $\hat{A}$, $\hat{B}$, and $\hat{\varepsilon}_\sigma$ are obtained in the zeroth order of $\chi_8^{\pm 3}$, $\chi_8^{\pm}$, and $\chi_7^{\pm}$, while a term with $C(z)$ is derived in the first order of $\chi_7^{\pm}$ and $\chi_8^{\pm}$ [19]. The term with $\hat{A}$ gives the $\hat{\boldsymbol{B}}_{\rm eff}^{\rm QW}$ component parallel to $(k_x, k_y, 0)$ which exists in the bulk $\boldsymbol{B}_{\rm eff}^{(p\text{-}d)}$ [Eq. (15)]. On the other hand, the term with $\hat{B}$, which is proportional to $d\tilde{\Gamma}_2(z)/dz$, introduces the $\hat{\boldsymbol{B}}_{\rm eff}^{\rm QW}$ component parallel to $(-k_y, k_x, 0)$. The term with $C(z)$ also gives the component in the direction of $(-k_y, k_x, 0)$ and represents the Rashba-type SOI, which includes a contribution from the p-d exchange interaction with $dB_{p\text{-}d}/dz$ in addition to that from the potential with dV_H/dz and $dh_{\rm w}/dz$, as shown in Appendix C. The z component of $\hat{\boldsymbol{B}}_{\rm eff}^{\rm QW}$ is induced by the spin dependence of the effective mass as in the bulk $\boldsymbol{B}_{\rm eff}^{(p\text{-}d)}$ [Eq. (15)]. The difference from the bulk is the z dependence of the effective mass which comes from $B_{p\text{-}d}(z)$.

V. NUMERICAL CALCULATION OF $\boldsymbol{k}\cdot\boldsymbol{p}$ HAMILTONIAN EIGENSTATES

By performing the numerical diagonalization of the eight-band $\boldsymbol{k}\cdot\boldsymbol{p}$ Hamiltonian [Eq. (3)], we calculate the spin splitting and the spin orientation in the conduction band for both the bulk and the QW. We explain features of the calculated numerical results by employing the analytical expressions of the bulk $\boldsymbol{B}_{\rm eff}^{(p\text{-}d)}$ and the QW $\hat{\boldsymbol{B}}_{\rm eff}^{\rm QW}$ derived in the previous section. We present calculated results in the $+z$ direction of magnetization for the purpose of comparing with analytical $\boldsymbol{B}_{\rm eff}^{(p\text{-}d)}$ and $\hat{\boldsymbol{B}}_{\rm eff}^{\rm QW}$ for this magnetization direction.

A. Procedures for numerical calculation

To obtain the spin orientation in each eigenstate of the $\boldsymbol{k}\cdot\boldsymbol{p}$ Hamiltonian, we use the spin matrix $\hat{\Sigma}_i$ in the basis set of Table I, which is given by

$$\hat{\Sigma}_i = \begin{bmatrix} \hat{\sigma}_i^{(s)} & O_{cv} \\ O_{cv}^\dagger & \hat{\sigma}_i^{(p)} \end{bmatrix}, \qquad i = x, y, z. \tag{26}$$

In the following calculated results, we denote this expectation value of the spin by $\langle\hat{\Sigma}_i\rangle$ to distinguish it from the expectation value calculated with respect to the eigenstate of the effective Hamiltonian [Eq. (14)], which is denoted as $\langle\hat{\sigma}_i\rangle_{\rm eff}$.

We use values of bulk band parameters shown in Table II, the fundamental energy gap E_g, the spin-orbit splitting Δ_g, and E_P [Eq. (21)] of the host semiconductor InAs [54]. For s-d and p-d exchange interactions $A_{s\text{-}d}$ and $B_{p\text{-}d}$, we use the values of $6A_{s\text{-}d} = 0.02$ eV and $6B_{p\text{-}d} = -0.22$ eV, which have been obtained in the first-principles calculation at the Fe^{3+} fraction of $x = 3.8\%$ [42], and for other values of x, we assume that $A_{s\text{-}d}$ and $B_{p\text{-}d}$ are proportional to x [Eq. (7)]. Although experimental values of $A_{s\text{-}d}$ and $B_{p\text{-}d}$ are missing in InFeAs, the sign and the magnitude of $A_{s\text{-}d}$ and $B_{p\text{-}d}$ are such that $A_{s\text{-}d} > 0$, $B_{p\text{-}d} < 0$, and $|A_{s\text{-}d}| \ll |B_{p\text{-}d}|$ have been confirmed experimentally and theoretically in GaMnAs [50]. Since $|A_{s\text{-}d}| \ll |B_{p\text{-}d}|$, we expect that the p-d exchange interaction will play a dominant role in spin physics and spintronics in InFeAs as well as GaMnAs. We find in the following that this is the case in the EMF as well as in the intrinsic anomalous Hall effect driven by the EMF, even for electrons in the conduction band with s symmetry at $\boldsymbol{k} = \boldsymbol{0}$, where the EMF by the p-d exchange interaction is induced through an additional process of the $\boldsymbol{k}\cdot\boldsymbol{p}$ interband transition.

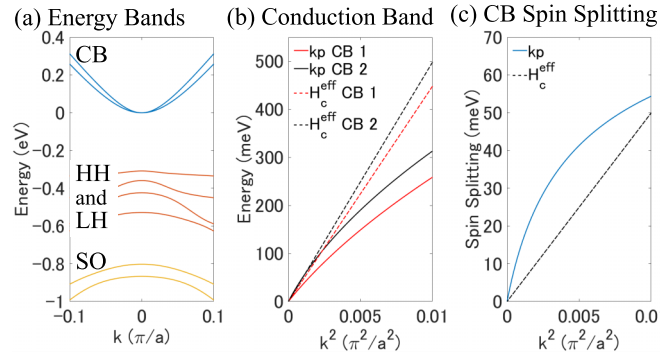

FIG. 5. (a) Energy bands, (b) the spin-split conduction bands, and (c) the spin splitting of the conduction bands in InFeAs at $x = 3.8\%$ (solid lines) calculated in the $\boldsymbol{k}\cdot\boldsymbol{p}$ Hamiltonian [Eq. (3)]. $\boldsymbol{k}$ is in the [101] direction, and a is the lattice constant of InAs. Parameter values are given in Table II. The s-d exchange interaction is not considered ($A_{s\text{-}d} = 0$). Dashed lines in (b) and (c) represent values obtained using $H_c^{\rm eff}$ [Eq. (14)].

In calculating eigenstates in the QW, we use a structure depicted in Fig. 3, which consists of the InFeAs well layer with width L_w and AlSb wall layers (the width of the whole QW structure is $2L$). Table II lists values of the band offset of the conduction band δ_6 [55], boundary potentials V_a and V_b, which determine the gate bias, and the doping profile (the density, ρ_a and ρ_b, the width w, and the position $\pm L_d$). The electron sheet density is determined by the charge neutrality to be $(\rho_a + \rho_b)w$. The electron distribution and the Hartree potential are determined self-consistently [17,19]. We can neglect the strain induced by the lattice mismatch between InAs and AlSb as in Ref. [56].

In most calculations, we neglect $A_{s\text{-}d}$ to clarify features of the spin splitting and the spin orientation brought by $B_{p\text{-}d}$. Later in Fig. 7, we present differences introduced by the presence of $A_{s\text{-}d}$.

B. Spin splitting and spin orientation in the bulk

In Fig. 5(a), we plot the energy of the conduction and valence bands in the vicinity of the zone center in the [101]

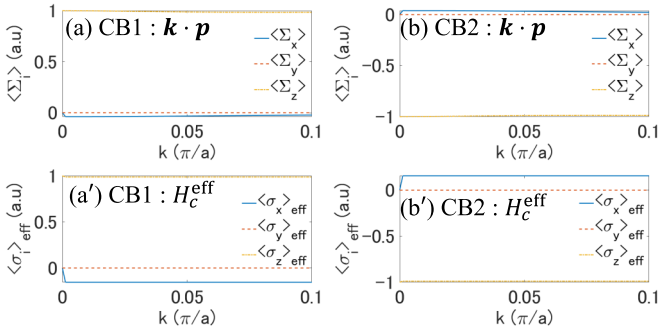

FIG. 6. Spin orientation indicated by expectation values of spin components $\langle\hat{\Sigma}_x\rangle$, $\langle\hat{\Sigma}_y\rangle$, and $\langle\hat{\Sigma}_z\rangle$ in the spin-split conduction bands (a) CB1 and (b) CB2 in Fig. 5(b), which are calculated using the $\boldsymbol{k}\cdot\boldsymbol{p}$ Hamiltonian. Also shown are $\langle\hat{\sigma}_x\rangle_{\rm eff}$, $\langle\hat{\sigma}_y\rangle_{\rm eff}$, and $\langle\hat{\sigma}_z\rangle_{\rm eff}$ in (a′) CB1 and (b′) CB2 obtained from the effective Hamiltonian [Eq. (14)]. More explanations are given in Fig. 5.

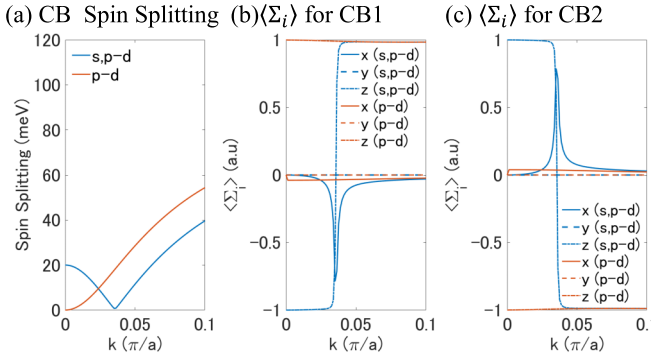

FIG. 7. (a) Spin splitting of the conduction band, and the spin orientation in (b) the lower spin state CB1 and (c) the upper spin state CB2 when $6A_{s\text{-}d} = 0.02$ (s, p-d, blue line) compared with those when $A_{s\text{-}d} = 0$ (p-d, red line). Other parameter values and $\boldsymbol{k}$ direction are identical to Fig. 5.

direction, which is calculated in the $\boldsymbol{k}\cdot\boldsymbol{p}$ Hamiltonian [Eq. (3)]. A close-up of the spin-split conduction bands is presented in Fig. 5(b), and the spin splitting as a function of the wave number k is shown in Fig. 5(c). Also plotted in Figs. 5(b) and 5(c) are the conduction-band energy and spin splitting (dashed lines) calculated in the effective Hamiltonian [Eq. (14)]. The spin splitting [Fig. 5(c)], which originates from the p-d exchange interaction in the present calculation at $A_{s\text{-}d} = 0$, shows a quadratic increase with the wave number k in the vicinity of $k = 0$ in the $\boldsymbol{k}\cdot\boldsymbol{p}$ calculation (solid line), in agreement with the k-quadratic spin splitting obtained analytically in Eq. (18) and plotted as a dashed line, while the rate of increase declines at a larger k in the $\boldsymbol{k}\cdot\boldsymbol{p}$ calculation. The value of the spin splitting reaches several tens of millielectronvolts at $k/(\pi/a) = 0.1$, with a the lattice constant of InAs. The Fermi wave number of $k_F/(\pi/a) = 0.1$ corresponds to the electron density of 10^{19} cm^{-3}, which is a typical value in experiments.

The conduction-band energy and spin splitting in the $\boldsymbol{k}\cdot\boldsymbol{p}$ calculation (solid line) deviates from those calculated in the effective Hamiltonian (dashed line). This is because we have only taken terms in the zeroth order of $\chi_8^{\pm 3}$, $\chi_8^{\pm}$, and $\chi_7^{\pm}$ in the effective Hamiltonian. Although retaining the higher-order terms will improve the quantitative accuracy, they bring unsolved eigenenergy E into the effective Hamiltonian. The simpler lowest-order effective Hamiltonian is useful enough to understand qualitative aspects of results in the $\boldsymbol{k}\cdot\boldsymbol{p}$ calculation. In Figs. 6(a) and 6(b), we show the spin orientation by plotting $\langle\hat{\Sigma}_i\rangle$, $i = x, y, z$, the expectation value of the 8×8 spin matrix $\hat{\Sigma}_i$ [Eq. (26)] with respect to each eigenstate in the spin-split conduction bands in Fig. 5(b). For comparison, Figs. 6(a′) and 6(b′) plot the expectation value of the Pauli spin matrix $\hat{\sigma}_i$ by the eigenstate of the effective Hamiltonian [Eq. (14)]. In each spin subband, $\langle\hat{\Sigma}_i\rangle$ and $\langle\hat{\sigma}_i\rangle$ have the same sign in each component, and the spin is nearly parallel or antiparallel to the magnetization. This can be understood by the analytical EMF $\boldsymbol{B}_{\rm eff}^{(p\text{-}d)}$ given in Eq. (15): the component of $\boldsymbol{B}_{\rm eff}^{(p\text{-}d)}$ parallel to the magnetization (along z), which only needs $B_{p\text{-}d}$, is larger than the perpendicular components, which require Δ_g in addition to $B_{p\text{-}d}$. In fact, the perpendicular component $\langle\hat{\Sigma}_x\rangle$ vanishes when $\Delta_g = 0$. The vanishing at $k_y = 0$ of $\langle\hat{\Sigma}_y\rangle$ shown in Fig. 6 is also consistent with the analytical expression of the y component of $\boldsymbol{B}_{\rm eff}^{(p\text{-}d)}$ in Eq. (15), which is proportional to k_y. The length of $\langle\hat{\Sigma}\rangle$ is slightly smaller from unity since the SOI in the valence band (Δ_g) flips the electron spin to reduce the average value [57].

Finally, we present the spin splitting and the spin orientation in the presence of the s-d exchange interaction $A_{s\text{-}d}$ to show that their essential features are the same as those in its absence except near $\boldsymbol{k} = \boldsymbol{0}$. Figure 7(a) presents the spin splitting of the conduction band, and Figs. 7(b) and 7(c) plot the spin orientation at $6A_{s\text{-}d} = 0.02$ for the $\boldsymbol{k}\cdot\boldsymbol{p}$ Hamiltonian. In the presence of $A_{s\text{-}d}$, the spin splitting almost vanishes at $k/(\pi/a) \simeq 0.03$, and the z component of the spin $\langle\hat{\Sigma}_z\rangle$ changes the sign there. This is explained by the direction reversal of the z component of the total EMF which occurs because the EMF, due to the positive $A_{s\text{-}d}$, is opposite in direction to $\boldsymbol{B}_{\rm eff}^{(p\text{-}d)}$ with the negative $B_{p\text{-}d}$ (Table II), and the magnitude of k-quadratic $\boldsymbol{B}_{\rm eff}^{(p\text{-}d)}$ increases with k. When $\langle\hat{\Sigma}_z\rangle$ changes the sign, the EMF is in the x direction, and $|\langle\hat{\Sigma}_x\rangle|$ approaches the unity. Despite such drastic changes brought by the s-d exchange interaction in the vicinity of $\boldsymbol{k} = \boldsymbol{0}$, the spin splitting and the spin orientation are mostly determined by the p-d exchange interaction at $k/(\pi/a) = 0.1$.

C. Spin splitting and spin orientation in the QW

Figure 8(a) presents the lowest spin-split subband of the conduction band in the vicinity of $k_x = k_y = 0$ along the k_x direction for both $B_{p\text{-}d} = 0$ and $B_{p\text{-}d} \neq 0$ when $A_{s\text{-}d} = 0$. In the case of $B_{p\text{-}d} = 0$, the Rashba SOI gives a spin splitting which is much smaller than the $B_{p\text{-}d}$-induced splitting and not visible in Fig. 8(a). The $B_{p\text{-}d}$-induced spin splitting is plotted in Fig. 8(b), which shows a quadratic increase with k as in the bulk [Fig. 5(c)]. In contrast to the bulk, the QW spin splitting is nonzero, even at $k_x = k_y = 0$. This zone-center spin splitting originates from the quantum confinement giving nonzero $\langle\hat{k}_z^2\rangle$, which leads to a spin-dependent kinetic energy at $k_x = k_y = 0$ when the effective mass is spin-dependent due to the p-d exchange interaction.

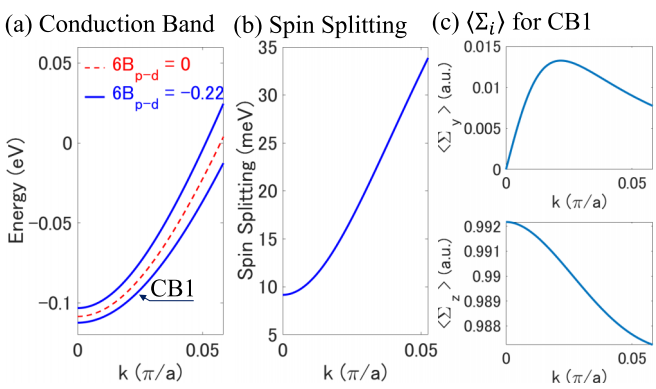

FIG. 8. (a) Lowest spin-split subband in the conduction band of the quantum well (QW; Fig. 3) when $6B_{p\text{-}d} = -0.22$ eV and $A_{s\text{-}d} = 0$ (blue solid line) with the spin splitting in (b) and the spin expectation values $\langle\hat{\Sigma}_y\rangle$ and $\langle\hat{\Sigma}_z\rangle$ of the lower spin state in (c) ($\langle\hat{\Sigma}_x\rangle$ is of the order of 10^{-11} and is not plotted). The wave vector (k_x, k_y) is in the vicinity of $k_x = k_y = 0$ along the k_x direction. For parameter values, see Table II. In (a), we also present the lowest subband when $B_{p\text{-}d} = 0$ and $A_{s\text{-}d} = 0$ (red dashed line), which also has the spin splitting, although it is not visible.

In Fig. 8(c), we present the spin orientation by plotting $\langle\hat{\Sigma}_y\rangle$ and $\langle\hat{\Sigma}_z\rangle$. The spin is oriented nearly in the direction of the magnetization (the z axis) as in the bulk (Fig. 6). This may be understood by the origin of the QW EMF $\hat{\boldsymbol{B}}_{\rm eff}^{\rm QW}$ in Eqs. (23)–(25): the component of $\hat{\boldsymbol{B}}_{\rm eff}^{\rm QW}$ parallel to the magnetization only needs the presence of $B_{p\text{-}d}$, while the terms with $\hat{A}$ and $\hat{B}$ in the perpendicular components require Δ_g in addition to $B_{p\text{-}d}$, and the term with $C(z)$ exists only in the presence of the inversion asymmetry and Δ_g.

VI. INTRINSIC ANOMALOUS HALL EFFECT IN THE BULK nFMS

As an example of transport properties reflecting the bulk p-d EMF $\boldsymbol{B}_{\rm eff}^{(p\text{-}d)}$ derived in Eq. (15), we present the calculated conductivity of the intrinsic anomalous Hall effect in this section. Here, $\boldsymbol{B}_{\rm eff}^{(p\text{-}d)}$ plays two roles, both of which are indispensable for the anomalous Hall effect [58]: one is the coupling of the spin of a conduction electron to the magnetization giving the broken time reversal symmetry, while the other is the coupling between the spin and the momentum of the conduction electron. Without $\boldsymbol{B}_{\rm eff}^{(p\text{-}d)}$ proposed in this paper, we would need the SOI, the Dresselhaus SOI [12] in the bulk case, in addition to the well-recognized s-d exchange interaction, to produce the anomalous Hall effect. Therefore, in this section, we also present the calculated anomalous Hall conductivity induced by the s-d exchange interaction and the Dresselhaus SOI to demonstrate a feature of the calculated $\boldsymbol{B}_{\rm eff}^{(p\text{-}d)}$-induced anomalous Hall conductivity. For this purpose, we do not consider the extrinsic contribution to the anomalous Hall conductivity.

A. Formula for the intrinsic anomalous Hall conductivity

The Hall conductivity of the intrinsic origin is given by [58]

$$\sigma_{xy} = -\frac{e^2}{\hbar}\sum_n \int \frac{d^3k}{(2\pi)^3} f(E_{n\boldsymbol{k}}) B^z_{n\boldsymbol{k}},$$

$$B^z_{n\boldsymbol{k}} = i\sum_{m(\neq n)} \frac{\langle n,\boldsymbol{k}|\frac{\partial H}{\partial k_x}|m,\boldsymbol{k}\rangle\langle m,\boldsymbol{k}|\frac{\partial H}{\partial k_y}|n,\boldsymbol{k}\rangle}{(E_{n\boldsymbol{k}} - E_{m\boldsymbol{k}})^2} + \text{c.c.}, \quad (27)$$

in which $B^z_{n\boldsymbol{k}}$ is the z component of the Berry curvature in the eigenstate $|n,\boldsymbol{k}\rangle$ of the Hamiltonian H at momentum $\hbar\boldsymbol{k}$ in the nth band with energy $E_{n\boldsymbol{k}}$, e is the elementary charge, $f(E)$ is the Fermi-Dirac distribution function, and c.c. means the complex conjugate of the preceding term. In calculating the $\boldsymbol{B}_{\rm eff}^{(p\text{-}d)}$-induced σ_{xy}, we employ the $\boldsymbol{k}\cdot\boldsymbol{p}$ Hamiltonian [Eq. (3)] for H in Eq. (27) since the effective Hamiltonian $H_c^{\rm eff}$ in Eq. (14) is no longer applicable at $x > 14\%$ in InFeAs.

In calculating σ_{xy} induced by the s-d exchange interaction and the Dresselhaus SOI, we use the following Hamiltonian:

$$H = \frac{\hbar^2k^2}{2m^*} + \boldsymbol{B}^{(D)}\cdot\hat{\boldsymbol{\sigma}} + 3A_{s\text{-}d}\hat{\sigma}_z,$$

$$B_i^{(D)} = \gamma_D k_i\left(k_j^2 - k_k^2\right),$$

$$(i,j,k) = (x,y,z),\ (y,z,x),\ \text{and}\ (z,x,y),$$

where m^* is the effective mass of the conduction band obtained by substituting $B_{p\text{-}d} = 0$ into $m^*_{\|\sigma}$ and $m^*_{z\sigma}$ in Eq. (19), and γ_D is the coefficient of the Dresselhaus SOI, for which we use the value of $\gamma_D = 0.0271$ eV nm^3 [1]. With this Hamiltonian, Eq. (27) gives

$$\begin{aligned}\sigma_{xy}^{(D)} = -\frac{e^2}{\hbar}\int\frac{d^3k}{(2\pi)^3}[f(E_+) - f(E_-)]\\ \times \frac{-\gamma_D^2}{2(\Delta E_D)^3}\{2\gamma_D k_z k_x^2\left(k_y^2 - k_z^2\right)\left(k_x^2 + 2k_y^2 - k_z^2\right)\\ + 2\gamma_D k_z k_y^2\left(k_z^2 - k_x^2\right)\left(2k_x^2 + k_y^2 - k_z^2\right)\\ + \left[\gamma_D k_z\left(k_x^2 - k_y^2\right) + 3A_{s\text{-}d}\right]\\ \times \left[\left(k_y^2 - k_z^2\right)\left(k_z^2 - k_x^2\right) + 4k_x^2k_y^2\right]\},\end{aligned} \quad (28)$$

$$E_\pm = \frac{\hbar^2k^2}{2m^*} \pm \Delta E_D,$$

$$\Delta E_D = \sqrt{\left[B_x^{(D)}\right]^2 + \left[B_y^{(D)}\right]^2 + \left[B_z^{(D)} + 3A_{s\text{-}d}\right]^2}. \quad (29)$$

B. p-d and s-d contributions to the Hall conductivity

Figure 9(a) presents the Hall conductivity σ_{xy} at zero temperature for the electron density of 10^{19} cm^{-3} (giving the Fermi energy $\varepsilon_{\rm F}$ of 0.7 eV in the absence of the spin splitting) in the following three cases: the nFMS with both $B_{p\text{-}d}$ and $A_{s\text{-}d}$, $\sigma_{xy}^{(p+s)}$ (blue solid line), that with $B_{p\text{-}d}$ only, $\sigma_{xy}^{(p)}$ (black dashed line), and that with the Dresselhaus SOI and $A_{s\text{-}d}$, $\sigma_{xy}^{(D)}$ (red line). In all three cases, the Hall conductivity increases with x in the small x region ($x < 0.5\%$) because the coupling of the conduction-electron spin with the magnetization grows

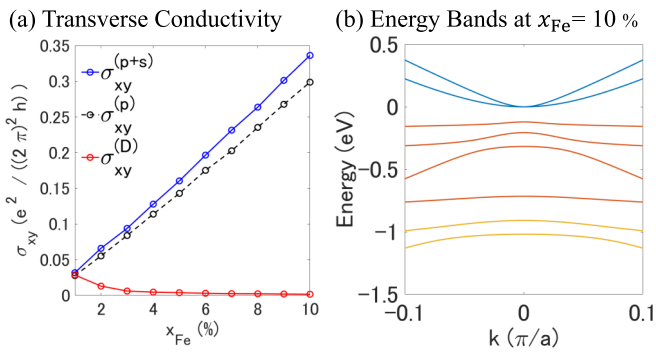

FIG. 9. (a) Intrinsic anomalous Hall conductivity of the n-type ferromagnetic semiconductor (nFMS) with both p-d and s-d exchange interactions $\sigma_{xy}^{(p+s)}$ (blue solid line), that with p-d exchange interaction only $\sigma_{xy}^{(p)}$ (black dashed line), and that with the Dresselhaus SOI and s-d exchange interaction $\sigma_{xy}^{(D)}$ (red line). (b) Energy bands in the [101] direction of the nFMS with p-d exchange interaction at $x = 10\%$.

with x. In the larger x region, however, as Fig. 9(a) ($x > 1\%$) shows, $\sigma_{xy}^{(D)}$ decreases with x, while $\sigma_{xy}^{(p)}$ and $\sigma_{xy}^{(p+s)}$ continue to increase with x.

The decrease of $\sigma_{xy}^{(D)}$ is due to the increase of the conduction-band spin splitting ΔE_D with x-linear $A_{s\text{-}d}$ [Eq. (29)]. In fact, Eq. (28) shows that $\sigma_{xy}^{(D)}$ approaches the $(A_{s\text{-}d})^{-1}$ dependence when $|\boldsymbol{B}^{(D)}| \ll 3A_{s\text{-}d} \ll \varepsilon_F$, considering the $A_{s\text{-}d}$ dependence of the integrand as well as the increase with $A_{s\text{-}d}$ in volume of the $\boldsymbol{k}$ region having $f(E_+) - f(E_-) \approx 1$.

On the other hand, the accelerated increase of $\sigma_{xy}^{(p)}$ and $\sigma_{xy}^{(p+s)}$ can be explained by the decrease of energy differences between conduction and valence bands. Figure 9(b) shows the energy band structure in the vicinity of $\boldsymbol{k} = 0$ at $x = 10\%$, which demonstrates that the bandgap gets narrower at such larger Fe fractions because of larger spin splittings in valence bands due to the exchange interaction $B_{p\text{-}d}$. Such a reduction of the energy differences leads to the enhancement of $\sigma_{xy}^{(p)}$ and $\sigma_{xy}^{(p+s)}$ at large x presented in Fig. 9(a), according to the expression of σ_{xy} in Eq. (27). This enhancement of the $B_{p\text{-}d}$-induced Hall conductivity is consistent with the expression Eq. (15) of the p-d EMF $\boldsymbol{B}_{\rm eff}^{(p\text{-}d)}$, which shows that the magnitude of $\boldsymbol{B}_{\rm eff}^{(p\text{-}d)}$, which is created with the interband transition across the bandgap (Fig. 1), increases as the energy denominator decreases.

VII. CONCLUSIONS

We have proposed a mechanism of the $\boldsymbol{k}$-dependent EMF in the conduction band induced by the exchange interaction in the valence band, based on a generalization of the $\boldsymbol{k}\cdot\boldsymbol{p}$ theory for the $\boldsymbol{k}$-dependent EMF in the conduction band induced by the SOI in the valence band. To demonstrate the importance of the exchange-induced EMF, we have considered the nFMS with the p-d exchange interaction in the valence band and evaluated the EMF in the conduction band of the bulk and the QW by numerically diagonalizing the eight-band $\boldsymbol{k}\cdot\boldsymbol{p}$ Hamiltonian based on the Zener model of the exchange interaction. We have also derived the effective Hamiltonian for an electron in the conduction band and obtained an analytical approximate EMF which we have used in understanding qualitative features of the spin splitting and the spin orientation. The lowest-order approximate EMF in the bulk is of the second order of the momentum since the exchange-induced EMF reverses the direction with the simultaneous reversal of the momentum and the magnetization. Consequently, in the QW with a nonzero quantized momentum perpendicular to the QW, the p-d exchange-induced EMF acquires a nonzero value at $k_x = k_y = 0$.

We have found that the conduction-band spin splitting created by the p-d exchange interaction in bulk nFMS of InFeAs reaches several tens of millielectronvolts at the Fermi momentum corresponding to the electron density of 10^{19} cm^{-3}, which exceeds the spin splitting produced by the s-d exchange interaction. In an nFMS QW, AlSb/InFeAs/AlSb, we have shown that the p-d exchange-induced spin splitting is much larger than a typical value of the Rashba spin splitting. This numerical estimation shows that the p-d exchange interaction is the dominant origin of the conduction-band EMF in an InFeAs nFMS. This suggests that the p-d exchange interaction is a promising source of the spin torque on the nFMS magnetization.

We have also calculated the intrinsic anomalous Hall conductivity generated by the p-d exchange interaction in a bulk InFeAs nFMS. In this anomalous Hall effect, both the coupling of the orbital to the spin of a conducting electron and that of the spin to the nFMS magnetization are provided by the p-d exchange interaction. The Hall conductivity created by the p-d exchange interaction exhibits an accelerated increase with the Fe dopant density, in contrast to that produced by the s-d exchange interaction and the Dresselhaus SOI, which shows a decrease except in the low dopant-density region.

Such a distinct feature in the anomalous Hall effect brought by the p-d exchange interaction in an nFMS suggests that the extended $\boldsymbol{k}\cdot\boldsymbol{p}$ mechanism of the $\boldsymbol{k}$-dependent EMF, presented in Fig. 1, is expected to promote the physics and application of the coupling between the spin and orbital degrees of freedom in a wide variety of materials and structures.

ACKNOWLEDGMENTS

This paper was supported by Grant-in-Aid for Scientific Research (C) Grant No. JP21K03413 from the Japan Society for the Promotion of Science. K.H. was partially supported by Hokkaido University DX Doctoral Fellowship (Grant No. JPMJSP2119).

APPENDIX A: ZENER MODEL IN FMSs

The Zener model of s-d and p-d exchange interactions [5,48–50,52] is a standard model for carrier-mediated ferromagnetism in FMSs. In this model, exchange interactions are treated as the interaction of s and p electrons with the magnetization produced by d electrons. This is valid when each of the s and p electrons interacts with many of the localized d-electron spins. Here, we demonstrate that it is the case in $In_{1-x}Fe_xAs$ at $x = 3.8\%$. The distance between Fe spins is 1.8 nm at this value of the Fe fraction, while the Fermi wavelength is 20 nm at the electron sheet density of

10^{12} cm^{-2} (Table II). In a QW with the well width of 20 nm, 10^3 Fe spins are present within the extent of each electron wave, and therefore, the coupling of the electron to localized Fe spins can be replaced by the interaction of the electron with the magnetization.

The carrier-mediated mechanism of the ferromagnetic phase in FMSs is supported by the observed increase of the Curie temperature T_c with the electron density [33]. In the Zener model of exchange interactions, Refs. [49,50] analytically show that T_c of the carrier-mediated ferromagnetic phase is proportional to the Fe concentration in the diluted limit. This dependence of T_c is in agreement with that in the density functional theory calculation [43]. Such a trend has also been confirmed in experiments: $T_c = 34$ K at $x = 5\%$ in a sample with the electron density of 1.8×10^{19} cm^{-3} [33], $T_c = 42$ and 65 K at $x = 6$ and 8%, respectively, in a sample with the electron density of 1×10^{19} cm^{-3} [37].

APPENDIX B: MATRICES IN THE INVARIANT EXPANSION OF THE KANE MODEL

The matrices $\boldsymbol{T}$ and $\boldsymbol{J}$ appearing in the invariant expansion of the $\boldsymbol{k}\cdot\boldsymbol{p}$ Hamiltonian [Eq. (3)] are given by [1]

$$T_x = \frac{1}{3\sqrt{2}}\begin{pmatrix} -\sqrt{3} & 0 & 1 & 0 \\ 0 & -1 & 0 & \sqrt{3} \end{pmatrix},$$

$$T_y = \frac{-i}{3\sqrt{2}}\begin{pmatrix} \sqrt{3} & 0 & 1 & 0 \\ 0 & 1 & 0 & \sqrt{3} \end{pmatrix},$$

$$T_z = \frac{\sqrt{2}}{3}\begin{pmatrix} 0 & 1 & 0 & 0 \\ 0 & 0 & 1 & 0 \end{pmatrix},$$

$$J_x = \frac{1}{2}\begin{pmatrix} 0 & \sqrt{3} & 0 & 0 \\ \sqrt{3} & 0 & 2 & 0 \\ 0 & 2 & 0 & \sqrt{3} \\ 0 & 0 & \sqrt{3} & 0 \end{pmatrix},$$

$$J_y = \frac{i}{2}\begin{pmatrix} 0 & -\sqrt{3} & 0 & 0 \\ \sqrt{3} & 0 & -2 & 0 \\ 0 & 2 & 0 & -\sqrt{3} \\ 0 & 0 & \sqrt{3} & 0 \end{pmatrix},$$

$$J_z = \frac{1}{2}\begin{pmatrix} 3 & 0 & 0 & 0 \\ 0 & 1 & 0 & 0 \\ 0 & 0 & -1 & 0 \\ 0 & 0 & 0 & -3 \end{pmatrix}.$$

APPENDIX C: RASHBA-TYPE SOI IN THE QW EFFECTIVE HAMILTONIAN

The coefficient of the Rashba-type SOI in Eqs. (23) and (24) is given by

$$\frac{P^2}{3}C(z) = \eta_B\frac{dB_{p\text{-}d}}{dz} + \eta_H\frac{dV_H(z)}{dz} - \eta_w\frac{dh_w}{dz},$$

with

$$\eta_B = \frac{P^2}{3}\frac{\Delta_g(18B_{p\text{-}d}+\Delta_g)}{\left[E_g(E_g+\Delta_g)-\Delta_g B_{p\text{-}d}-9B_{p\text{-}d}^2\right]^2},$$

$$\eta_H = \frac{P^2}{3}(\eta_2-\eta_1), \qquad \eta_w = \frac{P^2}{3}(\eta_2\delta_8-\eta_1\delta_7),$$

$$\eta_1 = \frac{(E_g-B_{p\text{-}d})(E_g+\Delta_g+B_{p\text{-}d})}{\delta_-}\frac{1}{E_g+\Delta_g+B_{p\text{-}d}} \times\left\{\frac{1}{E_g-B_{p\text{-}d}}-\frac{\Delta_g}{\delta_-}\right\},$$

$$\eta_2 = \frac{(E_g-B_{p\text{-}d})(E_g+\Delta_g+B_{p\text{-}d})}{\delta_-}\frac{1}{E_g-B_{p\text{-}d}} \times\left\{\frac{1}{E_g+\Delta_g+B_{p\text{-}d}}+\frac{\Delta_g}{\delta_-}\right\}.$$

[1] R. Winkler, *Spin-Orbit Coupling Effects in Two-Dimensional Electron and Hole Systems*, Springer Tracts in Modern Physics, Vol. 191 (Springer-Verlag, Berlin, 2003).

[2] S. Maekawa, S. O. Valenzuela, E. Saitoh, and T. Kimura, *Spin Current*, Vol. 22 (Oxford University Press, Oxford, 2017).

[3] A. Manchon, H. C. Koo, J. Nitta, S. M. Frolov, and R. A. Duine, New perspectives for Rashba spin-orbit coupling, Nat. Mater. **14**, 871 (2015).

[4] I. Žutić, J. Fabian, and S. D. Sarma, Spintronics: Fundamentals and applications, Rev. Mod. Phys. **76**, 323 (2004).

[5] T. Dietl and H. Ohno, Dilute ferromagnetic semiconductors: physics and spintronic structures, Rev. Mod. Phys. **86**, 187 (2014).

[6] J. Železný, P. Wadley, K. Olejník, A. Hoffmann, and H. Ohno, Spin transport and spin torque in antiferromagnetic devices, Nat. Phys. **14**, 220 (2018).

[7] T. Jungwirth, X. Marti, P. Wadley, and J. Wunderlich, Antiferromagnetic spintronics, Nat. Nanotechnol. **11**, 231 (2016).

[8] V. Baltz, A. Manchon, M. Tsoi, T. Moriyama, T. Ono, and Y. Tserkovnyak, Antiferromagnetic spintronics, Rev. Mod. Phys. **90**, 015005 (2018).

[9] J. Sinova, S. O. Valenzuela, J. Wunderlich, C. H. Back, and T. Jungwirth, Spin Hall effects, Rev. Mod. Phys. **87**, 1213 (2015).

[10] V. M. Edelstein, Spin polarization of conduction electrons induced by electric current in two-dimensional asymmetric electron systems, Solid State Commun. **73**, 233 (1990).

[11] A. Manchon, J. Železný, I. M. Miron, T. Jungwirth, J. Sinova, A. Thiaville, K. Garello, and P. Gambardella, Current-induced spin-orbit torques in ferromagnetic and antiferromagnetic systems, Rev. Mod. Phys. **91**, 035004 (2019).

[12] G. Dresselhaus, Spin-orbit coupling effects in zinc blende structures, Phys. Rev. **100**, 580 (1955).

[13] E. I. Rashba, Properties of semiconductors with an extremum loop. 1. Cyclotron and combinational resonance in a magnetic field perpendicular to the plane of the loop, Sov. Phys. Solid State **2**, 1109 (1960).

[14] F. J. Ohkawa and Y. Uemura, Quantized surface states of a narrow-gap semiconductor, J. Phys. Soc. Jpn. **37**, 1325 (1974).

[15] Y. A. Bychkov and E. I. Rashba, Oscillatory effects and the magnetic susceptibility of carriers in inversion layers, J. Phys. C **17**, 6039 (1984).

[16] E. O. Kane, Band structure of indium antimonide, J. Phys. Chem. Solids **1**, 249 (1957).

[17] R. Lassnig, k → ·p → theory, effective-mass approach, and spin splitting for two-dimensional electrons in GaAs-GaAlAs heterostructures, Phys. Rev. B **31**, 8076 (1985).

[18] E. Bernardes, J. Schliemann, M. Lee, J. C. Egues, and D. Loss, Spin-Orbit Interaction in Symmetric Wells with Two Subbands, Phys. Rev. Lett. **99**, 076603 (2007).

[19] R. S. Calsaverini, E. Bernardes, J. C. Egues, and D. Loss, Intersubband-induced spin-orbit interaction in quantum wells, Phys. Rev. B **78**, 155313 (2008).

[20] H. Akera, H. Suzuura, and Y. Egami, Spin relaxation in a quantum well by phonon scatterings, Phys. Rev. B **92**, 205311 (2015).

[21] H. Akera, H. Suzuura, and Y. Egami, Gate-voltage-induced switching of the Rashba spin-orbit interaction in a composition-adjusted quantum well, Phys. Rev. B **95**, 045301 (2017).

[22] J. Nitta, T. Akazaki, H. Takayanagi, and T. Enoki, Gate Control of Spin-Orbit Interaction in an Inverted $In_{0.53}Ga_{0.47}As/In_{0.52}Al_{0.48}As$ Heterostructure, Phys. Rev. Lett. **78**, 1335 (1997).

[23] T. Koga, J. Nitta, T. Akazaki, and H. Takayanagi, Rashba Spin-Orbit Coupling Probed by the Weak Antilocalization Analysis in InAlAs/InGaAs/InAlAs Quantum Wells as a Function of Quantum Well Asymmetry, Phys. Rev. Lett. **89**, 046801 (2002).

[24] T. Ishikawa and H. Akera, Antiparallel spin Hall current in a bilayer with skew scattering, Phys. Rev. B **100**, 125307 (2019).

[25] K. Hayashida and H. Akera, D'yakonov-Perel' spin relaxation in a bilayer with local structural inversion asymmetry, Phys. Rev. B **101**, 035306 (2020).

[26] T. Iijima, Y. Egami, and H. Akera, Suppressing effective magnetic field and spin-relaxation rate by tuning barrier compositions in a (111) quantum well, Jpn. J. Appl. Phys. **59**, 100901 (2020).

[27] T. Iijima and H. Akera, Gate-Voltage-Induced Switching of the Spin-Relaxation Rate in a Triple-Quantum-Well Structure, Phys. Rev. Applied **13**, 064075 (2020).

[28] J. Schliemann, Colloquium: Persistent spin textures in semiconductor nanostructures, Rev. Mod. Phys. **89**, 011001 (2017).

[29] M. Kohda, V. Lechner, Y. Kunihashi, T. Dollinger, P. Olbrich, C. Schönhuber, I. Caspers, V. V. Bel'kov, L. E. Golub, D. Weiss, K. Richter, J. Nitta, and S. D. Ganichev, Gate-controlled persistent spin helix state in (In, Ga)As quantum wells, Phys. Rev. B **86**, 081306(R) (2012).

[30] M. Naka, S. Hayami, H. Kusunose, Y. Yanagi, Y. Motome, and H. Seo, Spin current generation in organic antiferromagnets, Nat. Commun. **10**, 4305 (2019).

[31] M. Tanaka, Recent progress in ferromagnetic semiconductors and spintronics devices, Jpn. J. Appl. Phys. **60**, 010101 (2020).

[32] P. Nam Hai, L. Duc Anh, S. Mohan, T. Tamegai, M. Kodzuka, T. Ohkubo, K. Hono, and M. Tanaka, Growth and characterization of *n*-type electron-induced ferromagnetic semiconductor (In, Fe)As, Appl. Phys. Lett. **101**, 182403 (2012).

[33] P. Nam Hai, L. D. Anh, and M. Tanaka, Electron effective mass in *n*-type electron-induced ferromagnetic semiconductor (In,Fe)As: evidence of conduction band transport, Appl. Phys. Lett. **101**, 252410 (2012).

[34] L. Duc Anh, P. Nam Hai, and M. Tanaka, Control of ferromagnetism by manipulating the carrier wavefunction in ferromagnetic semiconductor (In, Fe)As quantum wells, Appl. Phys. Lett. **104**, 042404 (2014).

[35] M. Kobayashi, L. D. Anh, P. N. Hai, Y. Takeda, S. Sakamoto, T. Kadono, T. Okane, Y. Saitoh, H. Yamagami, Y. Harada, M. Oshima, M. Tanaka, and A. Fujimori, Spin and orbital magnetic moments of Fe in the *n*-type ferromagnetic semiconductor (In, Fe)As, Appl. Phys. Lett. **105**, 032403 (2014).

[36] D. Sasaki, L. D. Anh, P. Nam Hai, and M. Tanaka, Interplay between strain, quantum confinement, and ferromagnetism in strained ferromagnetic semiconductor (In, Fe)As thin films, Appl. Phys. Lett. **104**, 142406 (2014).

[37] L. D. Anh, P. N. Hai, and M. Tanaka, Observation of spontaneous spin-splitting in the band structure of an *n*-type zinc-blende ferromagnetic semiconductor, Nat. Commun. **7**, 13810 (2016).

[38] M. Kobayashi, L. D. Anh, J. Minár, W. Khan, S. Borek, P. N. Hai, Y. Harada, T. Schmitt, M. Oshima, A. Fujimori, M. Tanaka, and V. N. Strocov, Minority-spin impurity band in *n*-type (In,Fe)As: A materials perspective for ferromagnetic semiconductors, Phys. Rev. B **103**, 115111 (2021).

[39] M. Braun and U. Rössler, Magneto-optic transitions and non-parabolicity parameters in the conduction band of semiconductors, J. Phys. C: Solid State Phys. **18**, 3365 (1985).

[40] H. R. Trebin, U. Rössler, and R. Ranvaud, Quantum resonances in the valence bands of zinc-blende semiconductors. I. Theoretical aspects, Phys. Rev. B **20**, 686 (1979).

[41] G. L. Bir and G. E. Pikus, *Symmetry and Strain-Induced Effects in Semiconductors* (Wiley, New York, 1974).

[42] S. Sakamoto and A. Fujimori, Chemical trend in the electronic structure of Fe-doped III–V semiconductors and possible origin of ferromagnetism: A first-principles study, J. Appl. Phys. **126**, 173910 (2019).

[43] J.-Y. You, B. Gu, S. Maekawa, and G. Su, Microscopic mechanism of high-temperature ferromagnetism in Fe, Mn, and Cr-doped InSb, InAs, and GaSb magnetic semiconductors, Phys. Rev. B **102**, 094432 (2020).

[44] P. Zhang, Y.-H. Kim, and S.-H. Wei, Origin of High-TC Ferromagnetism in Isovalent-Doped III-V Semiconductors, Phys. Rev. Applied **11**, 054058 (2019).

[45] T. Fukushima, H. Shinya, A. Masago, K. Sato, and H. Katayama-Yoshida, Theoretical prediction of maximum Curie temperatures of Fe-based dilute magnetic semiconductors by first-principles calculations, Appl. Phys. Express **12**, 063006 (2019).

[46] H. Shinya, T. Fukushima, A. Masago, K. Sato, and H. Katayama-Yoshida, First-principles prediction of the control of magnetic properties in Fe-doped GaSb and InSb, J. Appl. Phys. **124**, 103902 (2018).

[47] G. Bastard, *Wave Mechanics Applied to Semiconductor Heterostructures* (Halsted, Les Ulis, France, 1988).

[48] J. K. Furdyna, Diluted magnetic semiconductors, J. Appl. Phys. **64**, R29 (1988).

[49] T. Dietl, H. Ohno, F. Matsukura, J. Cibert, and D. Ferrand, Zener model description of ferromagnetism in zinc-blende magnetic semiconductors, Science **287**, 1019 (2000).

[50] T. Dietl, H. Ohno, and F. Matsukura, Hole-mediated ferromagnetism in tetrahedrally coordinated semiconductors, Phys. Rev. B **63**, 195205 (2001).

[51] M. Abolfath, T. Jungwirth, J. Brum, and A. H. MacDonald, Theory of magnetic anisotropy in $III_{1-x}Mn_xV$ ferromagnets, Phys. Rev. B **63**, 054418 (2001).

[52] T. Jungwirth, J. Sinova, J. Mašek, J. Kučera, and A. H. MacDonald, Theory of ferromagnetic (III,Mn)V semiconductors, Rev. Mod. Phys. **78**, 809 (2006).

[53] T. Jungwirth, W. A. Atkinson, B. H. Lee, and A. H. MacDonald, Interlayer coupling in ferromagnetic semiconductor superlattices, Phys. Rev. B **59**, 9818 (1999).

[54] I. Vurgaftman, J. R. Meyer, and L. R. Ram-Mohan, Band parameters for III–V compound semiconductors and their alloys, J. Appl. Phys. **89**, 5815 (2001).

[55] A. Nakagawa, H. Kroemer, and J. H. English, Electrical properties and band offsets of InAs/GaSb*n*-*N* isotype heterojunctions grown on GaAs, Appl. Phys. Lett. **54**, 1893 (1989).

[56] F. Nichele, M. Kjaergaard, H. J. Suominen, R. Skolasinski, M. Wimmer, B.-M. Nguyen, A. A. Kiselev, W. Yi, M. Sokolich, M. J. Manfra, F. Qu, A. J. A. Beukman, L. P. Kouwenhoven, and C. M. Marcus, Giant Spin-Orbit Splitting in Inverted InAs/GaSb Double Quantum Wells, Phys. Rev. Lett. **118**, 016801 (2017).

[57] R. Winkler, Spin orientation and spin precession in inversion-asymmetric quasi-two-dimensional electron systems, Phys. Rev. B **69**, 045317 (2004).

[58] N. Nagaosa, J. Sinova, S. Onoda, A. H. MacDonald, and N. P. Ong, Anomalous Hall effect, Rev. Mod. Phys. **82**, 1539 (2010).